





Bufotalin-loaded biomimetic Prussian blue nanoparticles for colorectal cancer chemo-photothermal ferroptosis therapy

Yi Wu^{‡,1,3} , Jiahui Tian^{‡,1,2,3} , Jialu Yang¹, Qian Peng², Zhengchun Wu⁴, Rushi Liu^{2,3}, Mengjie Luo⁵, Yilan Qiu^{*,3,7} & Ruiyun Cao^{**,6}

¹The First Affiliated Hospital of Hunan Normal University, Changsha, 410013, China

²Department of Medical Laboratory, School of Medicine, Hunan Normal University, Changsha, 410013, China

³Immunodiagnostic Reagents Engineering Research Center of Hunan Province, Hunan Normal University, Changsha, 410013, China

⁴Hunan Cancer Hospital, Changsha, 410014, China

⁵Shenzhen Yantian District People's Hospital, Shenzhen, 518081, China

⁶Wujin Hospital of Traditional Chinese Medicine, Changzhou, 213161, China

⁷School of Life Science, Hunan Normal University, Changsha, 410013, China

*Author for correspondence: qiu730822@163.com

**Author for correspondence: 2523419791@qq.com

‡Authors contributed equally

Purpose: We constructed biomimetic nanoparticles with biocompatible, tumor-targeting, laser-responsive properties for ferroptosis-induced colorectal cancer chemo-photothermal therapy, with the aim to realize double-hit ferroptosis treatment for colorectal cancer. **Methods:** The nanoparticles were prepared by first loading the chemotherapy drug bufotalin (CS-5) with Prussian blue (PB), then combining a hybridized erythrocyte–tumor membrane (M) with PB@CS-5 to produce PB@CS-5@M. The chemo-photothermal therapy efficiency of PB@CS-5@M was tested by *in vitro* and *in vivo* experiments. **Results and conclusion:** The combined PB and CS-5 act as promising ferroptosis inducers to enhance ferroptosis efficacy. The hyperthermia induced by laser stimulation can trigger PB to release CS-5 and iron and ferrous ions, which further promotes ferroptosis.

First draft submitted: 20 October 2023; Accepted for publication: 9 November 2023; Published online: 10 January 2024

Keywords: bufotalin • chemo-photothermal therapy • colorectal cancer • ferroptosis • Prussian blue

Colorectal cancer is the world's third leading cancer and the second leading cause of cancer-related deaths worldwide [1–3]. The treatment of colorectal cancer includes surgery, radiotherapy, chemotherapy, targeted therapy and ablation. Although chemotherapy has made progress, the cure rate is far behind those of breast cancer and lung cancer, considering the liver and lung metastasis of colorectal cancer [3–6]. In addition, chemotherapy may result in serious adverse effects such as hematotoxicity and drug resistance, leading to a poor prognosis for patients [7–9]. Given this, there is an urgent need to develop a new treatment strategy for colorectal cancer.

Bufotalin (CS-5) is a natural compound derived from Chansu [10], a traditional Chinese medicine, which can effectively treat melanoma [11], lung cancer [12] and liver cancer [13]. Zhao *et al.* demonstrated that the mechanism of bufotalin killing tumor cells is to induce G2/M phase cell-cycle arrest and apoptosis, thereby inhibiting A375 cell proliferation [11]. Zhang *et al.* also proved that bufotalin inhibits the expression of GPX4 and promotes the production of reactive oxygen species (ROS) and the level of intracellular iron (Fe^{2+} form), thereby inducing ferroptosis and inhibiting the proliferation of A549 cells, which suggested the prospect of developing CS-5 as a novel ferroptosis inducer for antitumor therapy [12].

Ferroptosis is an iron-dependent mode of cell death triggered by the inactivation of glutathione-dependent antioxidant defenses, leading to the accumulation of toxic lipid ROS, which differs from other forms of cell death [14]. Its characteristics include increased ROS level, decreased GPX4 and damaged mitochondria [15,16]. In the latest study, the combination of siramesine and lapatinib was used to solve lapatinib resistance to breast cancer

therapy by inducing ferroptosis [17]. However, due to the high renal clearance and difficulty in accurately reaching the tumor sites, the clinical application prospects of many ferroptosis-inducing drugs have been limited [18]. It deserves mentioning that many nanomaterials were prepared to overcome these limitations. Due to their incomparable advantages, including non-toxicity, longer blood circulation time, tumor-homing ability, high drug-loading rate and controlled drug release, they provide a promise for specific ferroptosis cancer therapy [19–21]. Iron-based nanomaterials have gained advantages in inducing ferroptosis of cancer cells, due to their superiority of releasing iron and ferrous ions to induce ROS generation [18,22].

Prussian blue (PB), as an iron-based nanomaterial, possesses the advantages of a high drug-loading rate and excellent photothermal properties; more importantly, the US FDA has approved PB for the treatment of radiation diseases and MRI, because of its good biological safety [23,24]. Chen *et al.* constructed a triple therapy based on curcumin and 5-fluorouracil loaded with PB for colorectal cancer treatment [25]. Moreover, PB with laser irradiation can release iron and ferrous ions to promote ROS production, which is expected to further improve tumor cell ferroptosis in tumor therapy [26]. Until now, no studies have demonstrated the potential of CS-5 for colorectal cancer treatment by inducing tumor cell ferroptosis. PB for photothermal therapy (PTT) has the potential to induce ferroptosis. Therefore, a biomimetic nanosystem with near-infrared laser response was constructed to combine CS-5 with PB for chemo-photothermal therapy against colorectal cancer by inducing ferroptosis. PB@CS-5 (PC) was prepared by loading the chemotherapy drug CS-5 with the PB, and then PB@CS-5@M (PCM) was further prepared by combining a hybridized erythrocyte–tumor membrane (M) with PC. The hybridized membrane endows PCM with tumor-targeting properties and long circulation time. CD47 molecules on the erythrocyte membrane surface avoid immunogenic clearance, the half-life of the nanodrug in blood circulation is prolonged, and the tumor cell membrane is targeted in the same type. Much research has demonstrated the ideal therapeutic effect of nanomedicine by using mixed membranes [27,28]. Xiao *et al.* successfully constructed a nanodrug system for the treatment of cervical cancer, which used a hybrid membrane to wrap with PB nanoparticles of gambufotalin (CS-6) and indometacin (IND) [29].

In this work, PCM was designed to attenuate the cardiotoxicity of CS-5 and assist CS-5 in achieving efficient accumulation and release at the tumor site. CS-5 downregulates the expression of GPX4, reduces mitochondrial membrane potential (MMP) and increases ROS, thus inducing ferroptosis; PB directly killed tumor cells under laser stimulation and released iron and ferrous ions to boost ROS generation and ferroptosis, which realized a double-hit ferroptosis treatment for colorectal cancer. Moreover, the nanocomplexes downregulated the expression of HSP70 under laser stimulation to enhance the chemotherapy sensitivity of colorectal cancer cells to CS-5.

Materials & methods

Materials

$K_3[Fe(CN)_6] \cdot 3H_2O$ was purchased from Shanghai Aladdin Biochemical Technology Co., Ltd (Shanghai, China). Poly(N-vinylpyrrolidone) was purchased from Zhanyun Chemical Co., Ltd (Shanghai, China). CS-5 was acquired from Dalian Medical University (Dalian, China). Rhodamine was obtained from Sigma-Aldrich (MO, USA). The JC-1 kit and Reactive Oxygen Species Assay Kit were purchased from Beyotime Biotechnology (Shanghai, China). Methyl thiazolyl tetrazolium (MTT) and 4',6-diamidino-2-phenylindole (DAPI) were purchased from Solarbio Technology (Beijing, China). The Calcein/PI cell viability/cytotoxicity assay kit was obtained from Yeasen Biotechnology (Shanghai, China). Hematoxylin and eosin (H&E) staining solution was purchased from Biosharp Technology Co., Ltd (Hefei, China).

Cell lines & animals

HCT116, NIH-3T3 and SW480 cells were purchased from Dalian Meilun Biotechnology Co., Ltd (Dalian, China). Human vascular smooth muscle cells and RAW 264.7 cells were obtained from Xiangya Central Laboratory (Changsha, China). Female nude BALB/c mice (4–5 weeks old) were obtained from SJA Laboratory Animal Co., Ltd (Hunan, China).

Synthesis of PB nanoparticles

PB nanoparticles (PBNPs) were synthesized according to the previous method [30]. First, 7.5 g poly(N-vinylpyrrolidone) and 330 mg $K_3[Fe(CN)_6] \cdot 3H_2O$ were weighed and dissolved in 0.1 M 100 ml HCl, and stirred at 800 r.p.m. for 1 h, then placed in an oil bath at 80°C for 20 h. PBNPs were collected after centrifugation, washing and freeze-drying.

Preparation of PCM

Preparation of red blood cell (RBC) membranes (RBCMs) was performed as previously reported [31]. Briefly, fresh blood collected from healthy mice was washed with phosphate-buffered saline (PBS; pH 7.4) five times. The RBC layer was collected and mixed with 25% PBS (pH 7.4) and lysed on ice for 2 h. Subsequently, the cracked RBCs were centrifuged at $12,000 \times g$ and washed until the supernatant was colorless, then stored at -80°C until use.

HCT116 cell membranes (HCTMs) were prepared according to instructions of the membrane protein extraction kit (Beyotime Biotechnology) [32]. HCT116 cells were scraped down and washed with PBS (pH 7.4), then the cells were centrifuged at $800 \times g$ and the precipitate was collected and resuspended in reagent A. Next, after five repeated freeze–thaw cycles, the samples were centrifuged at $800 \times g$, the supernatant was collected and centrifuged at $12,000 \times g$, and the precipitate of cell membranes was collected and stored at -80°C until use.

The preparation of the RBC–HCT hybrid membrane (RBC–HCTm) was as follows. After ultrasonication of RBCMs and HCTMs, they were filtered with a $0.22\text{-}\mu\text{m}$ filter membrane and then mixed at a ratio of 1:1.

For the preparation of PCM, $950\text{ }\mu\text{l}$ of PB (1 mg/ml) and $50\text{ }\mu\text{l}$ of CS-5 (1 mg/ml) were mixed and stirred at 800 r.p.m. for 12 h, then the mixture was centrifuged at $13,500 \times g$ for 15 min and the precipitate of PC was collected. Then 1 ml PC (1 mg/ml) and 1 ml RBC–HCTm (1 mg/ml) were mixed and stirred at 37°C for 2.5 h, then the mixture was centrifuged and PCM was acquired.

Characterization

Transmission electron microscopy was performed to capture the image of PB and PCM using a JEM-2100 microscope (JEOL, JPN, 200 kV). The size and ζ -potential of PB, PC and PCM were determined by Zetasizer Nano ZS (Malvern Instruments, Malvern, UK). UV-Vis spectrophotometry (Beckman Coulter, Inc., CA, USA) was conducted to detect the characteristic absorption peaks of PB, CS-5, PC and PCM. RBC–HCT116 membrane fusion was characterized by a laser confocal microscope (FV1000, Olympus, Tokyo, Japan). Membrane proteins including RBCm, HCTm, RBC–HCTm and PCM were determined by SDS-PAGE.

Photothermal performance characterization

Temperature change curve and infrared thermal images of PBS, PB, PC and PCM (0.2 mg/ml) after 808-nm laser irradiation ($1.2\text{ W}/\text{cm}^2$, 5 min) were recorded by the FLIR C2 infrared camera (Thermor Fisher Scientific Inc., USA). The temperature change curve of PCM at different concentrations was also measured to evaluate the temperature-rising capability. The photothermal curve of 0.5 ml PCM (0.2 mg/ml) was designed to calculate photothermal conversion efficiency. The photostability of PCM was evaluated by laser on/off for six cycles, and the characteristic peaks before and after laser irradiation were measured by UV-Vis spectrophotometry.

Evaluation of biocompatibility

The toxicity of PB and PBM (PB@M) to different cells (HCT116 cells, SW480 cells, NIH-3T3 cells and vascular smooth muscle cells) was detected by MTT assay. Briefly, when the cell density reached 80% in 96-well plates, different concentrations of PB and PBM (0, 12.5, 25, 50 and $100\text{ }\mu\text{g}/\text{ml}$) were added to the Petri dish and treated for 24 h, then the absorption peak at 490 nm was detected by MTT assay and the cell activity was calculated.

The hemolysis rates of RBCs in different samples were determined by spectrophotometry. PB, PC and PCM were added into 4% suspended RBCs to the final concentrations of 0, 25, 50, 100 and $200\text{ }\mu\text{g}/\text{ml}$. In addition, the positive control was treated with ddH_2O , and the negative control was treated with PBS. After incubation at 37°C for 6 h and centrifugation at $3000 \times g$ (5 min, 4°C), the absorbance of the supernatant at 540 nm was detected with a microplate reader. The hemolysis rate was calculated and RBC morphology was observed under the microscope.

Platelets extracted from fresh whole blood were incubated with PB, PC and PCM ($200\text{ }\mu\text{g}/\text{ml}$) at 37°C for 4 h. A thrombin treatment group was used as the positive control, and a PBS treatment group was used as the negative control. The absorbance of all samples at 650 nm was detected and the coagulation rate was calculated.

Cell uptake & immune escape assay

For the cell uptake assay, HCT116 cells were seeded into a 12-well plate and cultured. When the cell density reached 60%, $40\text{ }\mu\text{g}/\text{ml}$ of rhodamine-labeled PB coated with the hybrid membrane (PB@M^{Rho}) was added at 0, 2, 4, 6 and 8 h. The nuclei were stained with DAPI, and the images were captured by laser confocal microscopy.

For the immune escape assay, RAW 264.7 cells (5×10^4) were seeded into a 12-well plate and cultured overnight, then PB^{Rho} and PB@M^{Rho} (0, 25, 50 and 100 $\mu\text{g/ml}$) were added and cultured for 6 h. The nuclei were stained with DAPI, and the cells were imaged through the laser confocal microscope.

Antitumor effect & mechanism *in vitro*

For the cell viability assay, HCT116 cells were placed into a 96-well plate at a density of 8×10^3 per well and cultured for 24 h, and then treated with PBS, CS-5, PB, PC, PCM, PB + laser (L), PC + L or PCM + L (PB: 30 $\mu\text{g/ml}$; CS-5: 0.0889 $\mu\text{g/ml}$;), laser (L) represented that the group was treated with laser treatment. Laser irradiation was performed after 6 h (808 nm, 1.2 W/cm², 5 min), then cells were incubated for a further 18 h. Cell viability was detected by MTT assay.

For live–dead staining, HCT116 cells were seeded and cultured in 24-well plates for 24 h, then treated with PBS, CS-5, PB, PC or PCM, with or without laser (PB: 30 $\mu\text{g/ml}$; CS-5: 0.0889 $\mu\text{g/ml}$). The cells were stained with a Calcein AM/PI kit and imaged with the laser confocal microscope.

For ROS detection, when the HCT116 cells' confluence in 24-well plates reached 60%, they were treated with PBS, CS-5, PB, PC or PCM, with or without laser (PB: 30 $\mu\text{g/ml}$; CS-5: 0.0889 $\mu\text{g/ml}$). After incubation with the DCFH-DA probe for 30 min, the cells were imaged under a fluorescence microscope.

For detection of MMP, HCT116 cells were cultured in a 12-well plate, then treated with PBS, CS-5, PBM + L, PCM or PCM + L (PB: 30 $\mu\text{g/ml}$; CS-5: 0.0889 $\mu\text{g/ml}$). Laser irradiation was performed about 6 h later and then cells were incubated for 18 h, then stained with the JC-1 kit for 20 min and then imaged by laser confocal microscopy.

For western blotting, when the HCT116 cells' confluence in six-well plates reached 60%, they were treated with PBS, PB, PB + L, CS-5, PCM or PCM + L (PB: 30 $\mu\text{g/ml}$; CS-5: 0.0889 $\mu\text{g/ml}$). Cells were washed with PBS and cracked to extract proteins. The expression levels of C-caspase-3, p53, Bax and Bcl-2 were detected to evaluate the level of apoptosis, and the level of ferroptosis was evaluated by measuring the expression levels of GPX4 and HIF-1 α . In addition, the cells were treated with PBS, PB, PB + L, PBM + L, PC + L, or PCM + L, and the protein was extracted to evaluate the expression of HSP70.

Biodistribution & pharmacokinetics *in vivo*

When the tumor volume of female nude BALB/c mice reached 250 mm³, 100 μl of PB^{Ce6} or PB@M^{Ce6} (dose of PB = 5 mg/kg) were injected into mice by tail vein injection. Fluorescence imaging of tumor-bearing BALB/c mice was performed at 2, 4, 6, 8, 12, 24 and 48 h. The mice were dissected after 48 h and the heart, liver, spleen, lung, kidney and tumor were collected for imaging.

For the pharmacokinetic study, 200 μl of Ce6, PB^{Ce6} or PB@M^{Ce6} (dose of PB = 5 mg/kg) were injected into tumor-bearing BALB/c mice by tail vein injection. Blood samples were collected at 0, 1, 2, 4, 6, 8, 12 and 24 h after injection. After centrifugation at $3600 \times g$ for 5 min, the supernatant was collected for fluorescence imaging and the half-life of different samples was calculated.

Antitumor effect *in vivo*

To measure the antitumor effect, 100 μl HCT116 cells were first subcutaneously implanted on the back of female nude BALB/c mice at a density of 5×10^6 . When the tumor volume reached 100 mm³, the mice were randomly divided into five groups: PBS, PBM + L, CS-5, PCM and PCM + L ($n = 5$ per group). After the body weight and tumor size were recorded, the mice were treated via the tail vein with 100 μl PBS, PBM, CS-5 or PCM (doses: PB = 5 mg/kg; CS-5 = 1 mg/kg) and laser therapy was performed 12 h later. The dose of CS-5 was determined as 1 mg/kg to ensure its safety margin in chemotherapy and optimal efficacy for tumor ablation. Significant changes in tumor volume were observed in tumor-bearing mice after eight treatment cycles. The mice were euthanized, and the fresh blood of the mice was taken for the routine blood and biochemical tests. The heart, liver, spleen, lung, kidney and tumor were taken for tissue sections and then stained using H&E, immunohistochemistry and terminal deoxynucleotidyl transferase dUTP nick end labeling (TUNEL).

Analysis of the 16S rRNA gene sequence

Normal female nude BALB/c mice (as the control group) and female tumor-bearing BALB/c mice were treated with PBS and PCM + L as PBS and PCML groups, respectively ($n = 5$). The feces from three groups of mice were collected for 16S rRNA analysis (lc-bio, Hangzhou, China). All data were analyzed through R software (v.

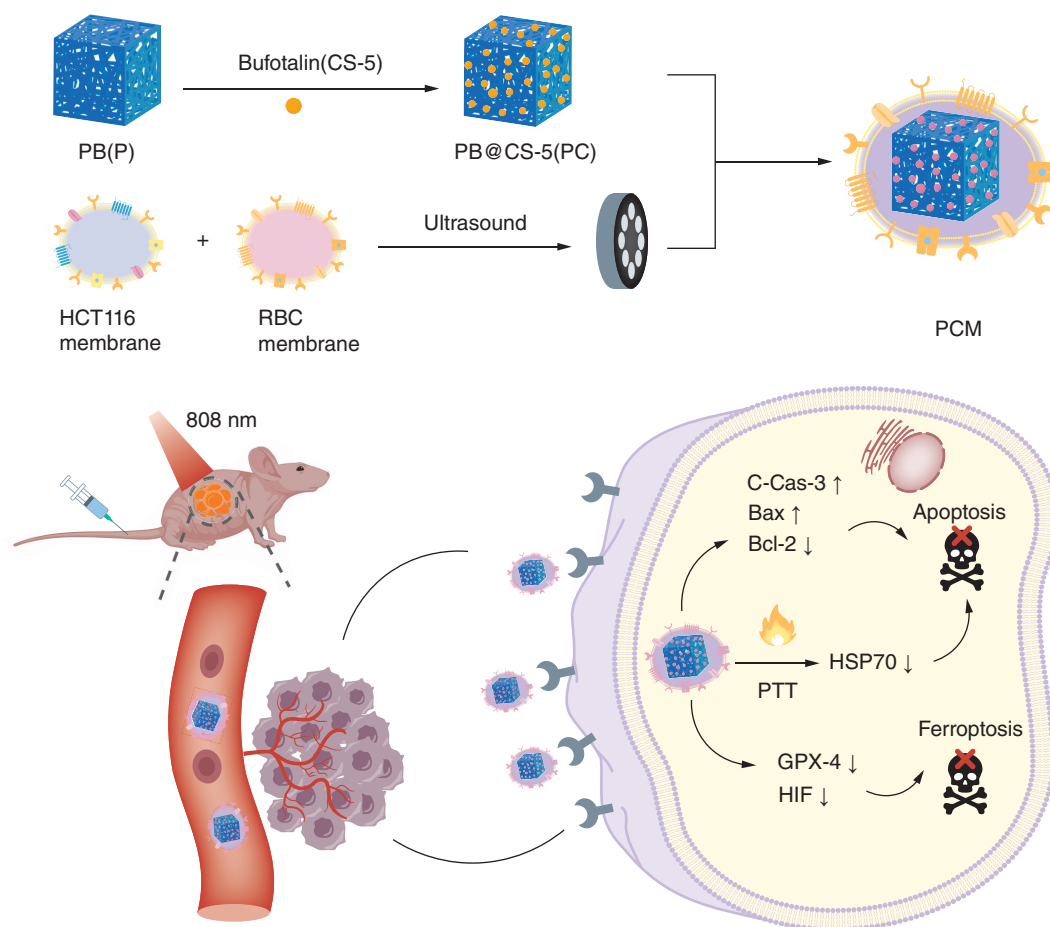


Figure 1. The synthesis procedures of buftotalin–Prussian blue biomimetic nanoparticles and mechanism of nanoparticle-induced ferroptosis for colorectal cancer chemo-photothermal therapy. CS-5: Buftotalin; PB: Prussian blue; PCM: Buftotalin–Prussian blue biomimetic nanoparticle; PTT: Photothermal therapy; RBC: Red blood cell.

3.6.3; R Foundation for Statistical Computing, Vienna, Austria) and the OmicStudio tools at www.omicstudio.cn. Correlation calculation was conducted with Pearson and Spearman correlation coefficients.

Statistical analysis

All values are presented as mean \pm standard deviation. The statistical difference between the two groups was calculated by *t*-test, and statistical differences above the two groups were performed by one-way analysis of variance using GraphPad Prism 8 software (v. 8.4.0; GraphPad, Inc., CA, USA). Statistical significance was set at **p* < 0.05, ***p* < 0.01 and ****p* < 0.001.

Results

Characterization of the PCM

The synthesis procedures of PCM are illustrated in Figure 1. The transmission electron microscopy image of PB shows its cube structure and 100-nm nanoparticle size with excellent dispersibility (Figure 2A). After loading with CS-5 and wrapping with the hybrid membrane, the transparent film surrounding the cuboid PBNPs shows that the hybrid membrane successfully wraps the PC inside, and the particle size of PCM is stable at about 100 nm (Figure 2B). In addition, dynamic light scattering analysis (DLS) demonstrated the average hydration diameters of PB, PC and PCM to be 98.49, 110.4 and 128.3 nm, respectively (Figure 2C). The ζ -potential measurement showed the negative charge of PBNPs. Due to the positive charge on the surface of CS-5, after loading with CS-5, the potential of PC increased significantly from -25.4 ± 1.14 mV to -10.1 ± 0.08 mV (Figure 2D); UV-Vis spectra

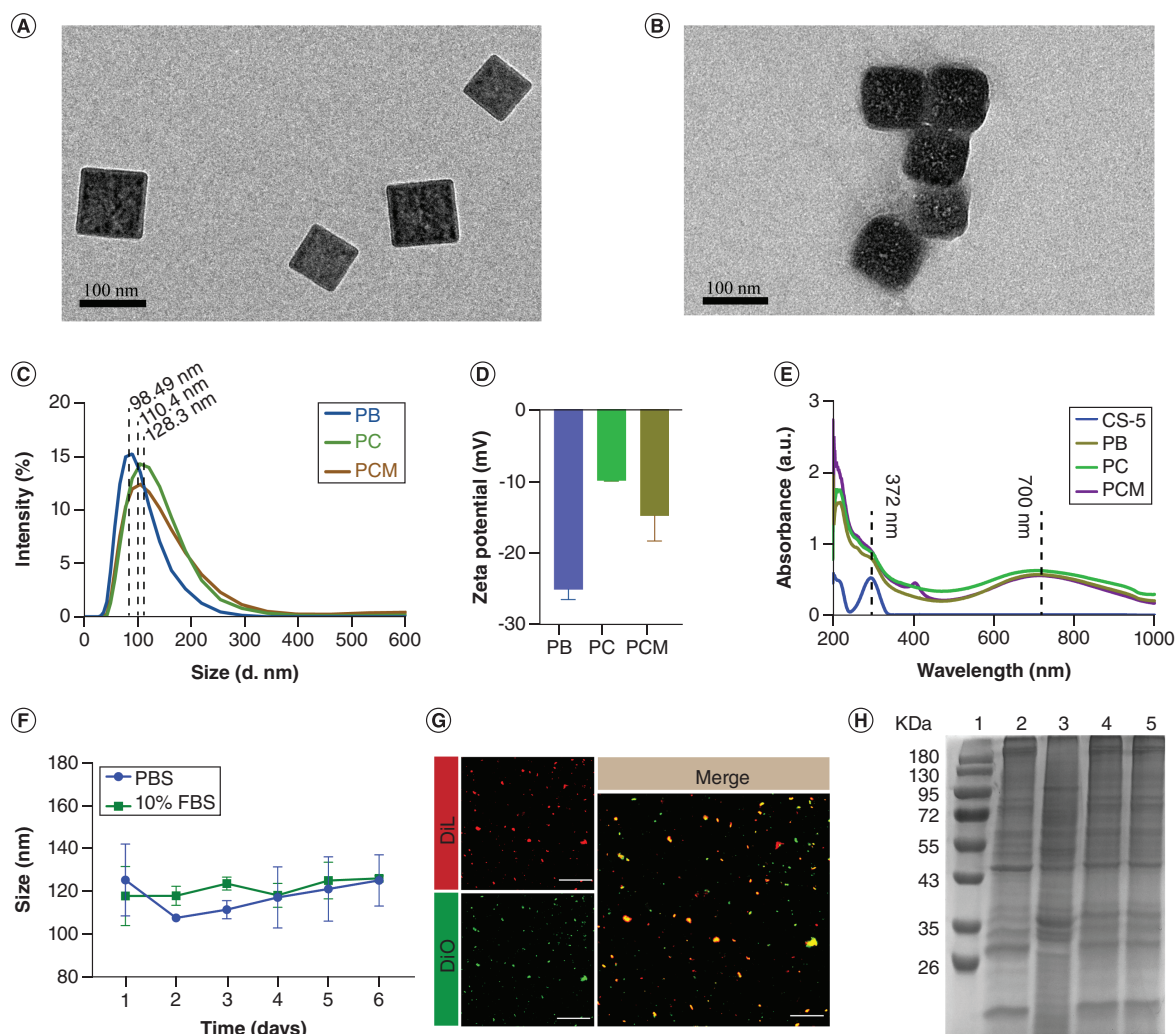


Figure 2. Characterization of the bufotalin-Prussian blue biomimetic nanoparticles. (A) Transmission electron microscopy image of PBNPs (scale bar = 100 nm). (B) Transmission electron microscopy image of PCM (scale bar = 100 nm). (C) Dynamic light scattering analysis of PB, PC and PCM. (D) ζ -potential analysis of PB, PC and PCM. (E) UV-Vis spectra of PB, CS-5, PC and PCM. (F) The stability analysis of PCM in phosphate-buffered saline and 10% fetal bovine serum for 6 consecutive days. (G) The fusion of RBCm and HCTm under laser scanning confocal microscope. (Dil labeled membrane = RBCm; Dio labeled membrane = HCTm; scale bar = 5 μ m). (H) SDS-PAGE analysis of RBCm (2), HCT116 m (3), RBC-HCTm (4), PCM (5).

CS-5: Bufotalin; Dil: Red fluorescence probe for cell membrane; Dio: Green fluorescence probe for cell membrane; HCTm: HCT116 cell membrane; PB: Prussian blue; PBNP: Prussian blue nanoparticle; PBS: 1 \times Phosphate-buffered saline; PC: Bufotalin-Prussian blue nanoparticle; PCM: Bufotalin-Prussian blue biomimetic nanoparticle; RBCm: Red blood cell membrane.

indicated the two absorption peaks of PC and PB at 700 (PB) and 372 nm (CS-5) (Figure 2E). This result showed that CS-5 was successfully loaded into PB. The UV-Vis spectrum of PCM displayed the characteristic peak of RBC-HCTm at 416 nm. Moreover, coating with RBC-HCTm directly resulted in the potential reduction of PCM (Figure 2D & E).

Monitoring the stability of PCM in 10% fetal bovine serum and PBS for 6 consecutive days, we found that the average particle size of PCM was stable between 120 and 130 nm (Figure 2F), indicating its excellent stability. When the mass ratio of PB to CS-5 was 1:1, the encapsulation efficiency and loading efficiency of PB to CS-5 were approximately 60%, which indicates the high drug-loading efficiency of CS-5 in PB (Supplementary Figure 1A). We further investigated the effects of laser and pH value on the release of CS-5 from PCM. The results indicated that the cumulative release of CS-5 from PCM at pH 7.4 was only 46.19% after 72 h, while the cumulative release of CS-5 reached 97.59% at pH 5.4 with laser irradiation (Supplementary Figure 1B). In addition, the release rate

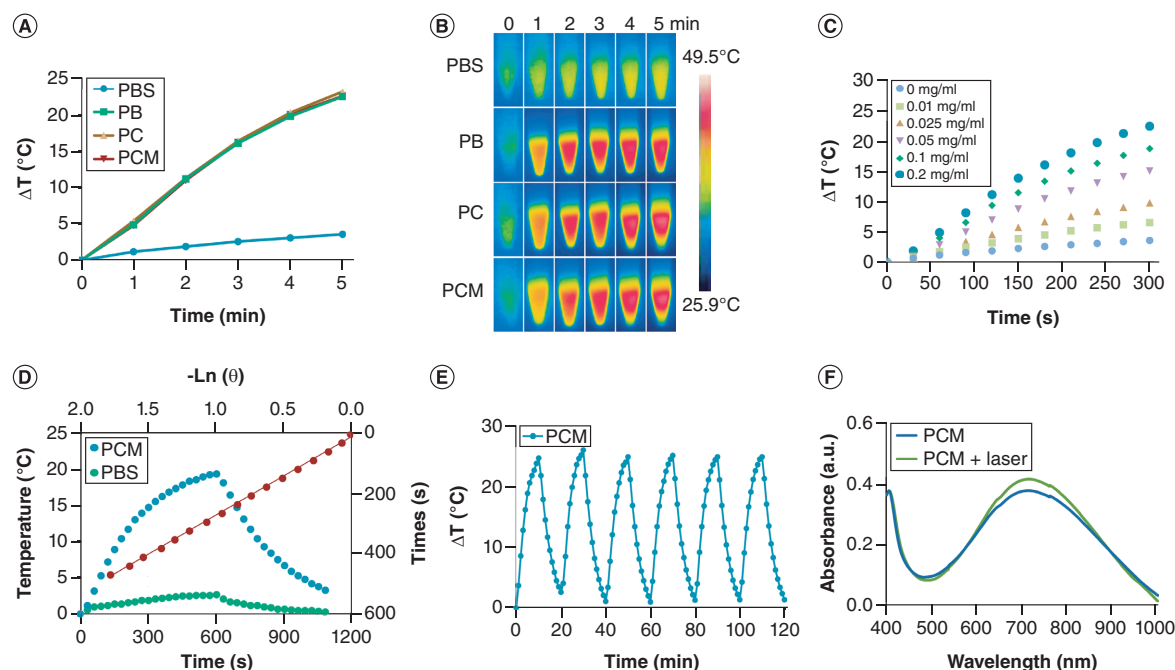


Figure 3. Photothermal performance characterization. (A) Temperature change and (B) infrared thermal images of different samples after 808-nm laser irradiation (1.2 W/cm², 5 min) (PB/PC/PCM: 0.2 mg/ml). (C) Photothermal performance of PCM with different concentrations (1.2 W/cm², 5 min). (D) The photothermal curve of PCM after 808-nm laser irradiation (0.8 W/cm², 5 min) (PCM: 0.1 mg/ml). (E & F) Photostability and UV-Vis spectra of PCM before and after six laser irradiation cycles (PCM: 0.2 mg/ml). PB: Prussian blue; PBS: 1 × Phosphate-buffered saline; PC: Bufotalin–Prussian blue nanoparticle; PCM: Bufotalin–Prussian blue biomimetic nanoparticle.

of CS-5 under 808-nm laser irradiation was increased significantly (44.1 vs 7.56%) (Supplementary Figure 1C). After RBCm and HCTm were labeled with red fluorescence probe for cell membranes (DiI) and green fluorescence probe for cell membranes (DiO), respectively, we performed a fusion assay of RBCm and HCTm. As we expected, yellow fluorescence (merged red and green fluorescence) under laser scanning confocal microscopy was observed due to the successful fusion of RBCm and HCTm (Figure 2G). In addition, the SDS-PAGE results showed that the integrity of membrane proteins in PCM was consistent with that of other groups (Figure 2H).

Photothermal performance characterization

The photothermal performance of PB is crucial for tumor PTT [26]. By monitoring the temperature-rising curves of PBS, PB, PC and PCM under laser irradiation (808 nm, 1.2 W/cm²) for 5 min, it was found that the temperature of PB, PC and PCM increased from 27 to 49.5°C (Figure 3A & B), higher than the temperature required to kill tumor cells (42°C) [33]. In addition, the photothermal effect of PCM was concentration-dependent (Figure 3C). It should be noted that CS-5 and hybrid membrane did not affect the photothermal properties of PB. Furthermore, the photothermal conversion efficiency of the PCM was 31.33% (Figure 3D), which is higher than that of SQ1 nanoprobe ($\eta = 25.6\%$) [34] and Au nanorods ($\eta = 23.7\%$) [35]. As the long-term photothermal effect of PB on tumor sites has great potential for its application in targeted tumor therapy [36], we then investigated the photothermal stability. Figure 3E & F indicate that the maximum temperature peak and the UV-Vis spectrum of PCM remain unchanged after six cycles of laser on/off irradiation. The above results demonstrate that PB is an excellent photothermal agent for PTT due to its excellent photothermal properties and stability. It suggests that it has a good prospect of application in tumor treatment.

Biocompatibility of PCM *in vitro*

Although the FDA has proven that PB has excellent safety as an antidote [37], biomembranes with excellent biocompatibility also contribute to the clinical transformation of nanomaterials [38,39]. In this study, the cytotoxicity analysis of PB and PBM on HCT116 cells, SW480 cells, vascular smooth muscle cells and NIH-3T3 cells indicated

that even if the concentration of PB was as high as 100 $\mu\text{g/ml}$, the cell viabilities of the PBM group and PB group were 85 and 80%, respectively (Supplementary Figure 2A & B). In addition, compared with the positive group, the other groups did not affect the hemolysis rate, which with PCM was 2.97% and with PC was 4.12%; even at the highest concentration of PB (200 $\mu\text{g/ml}$), there were no significant changes in RBC morphology (Supplementary Figure 2C & D). There was also no difference in coagulation rate between different materials groups (Supplementary Figure 2E). These results indicate that different materials have no significant effect on hemolysis and coagulation, and also show that PCM has excellent biocompatibility with no toxic side effects, which is conducive to further clinical trials *in vivo*.

Cell uptake & immune escape assay

Cell uptake efficiency and immune escape assay were used to evaluate the practical potential of PCM *in vivo*. PCM was labeled with Ce6, a fluorophore that can emit red fluorescence. Red fluorescence intensity in the cytoplasm represents the uptake of substances by cells. The results in Supplementary Figure 3A showed that the uptake of PBM in macrophages was significantly lower than that of PB with the same concentration ($p < 0.001$ and $p < 0.01$). As shown in Supplementary Figure 3B, the low uptake of PCM in macrophages revealed that the weak immune response is caused by the immune-escaping ability of the hybrid membrane, which helps prolong blood circulation time. In addition, by evaluating the uptake of PBM in HCT116 cells at different time points, it was found that the red fluorescence gradually increased with time extension, but remained stable after 6 h (Supplementary Figure 3C & D). Therefore, the optimal laser irradiation time was determined at 6 h to ensure the highest photothermal efficiency.

Antitumor effect & mechanism *in vitro*

Next, we investigated the photothermal killing effect of PB on HCT116 cells when the concentration of PB was 30, 40 and 50 $\mu\text{g/ml}$. The kill effects of PB at these different concentrations were 16.6, 59.6 and 83.3%, respectively, indicating that 30 $\mu\text{g/ml}$ of PB was the optimal concentration for combinational therapy (Supplementary Figure 4). Then the cell killing rates of PB + L, PC and PC + L (PB = 30 $\mu\text{g/ml}$; PB:CS-5 = 15:1) on HCT116 cells were measured. The results indicated that the combined efficacy of PC + L (85.3%) was better than that of the stacking effect of PC (63.9%) or PB plus the laser (16.6%) (Figure 4A). In addition, compared with PC + L, the cell killing rate of PCM + L was slightly reduced, which may help the slow release of CS-5 from PC after coating with hybrid membrane (Figure 4B). In addition, the effect of chemo-photothermal therapy of PCM *in vitro* was verified by living/dead staining, in which green fluorescence and red fluorescence represent living cells and dead cells, respectively. Compared with other groups, strong red fluorescence reflected the significant killing effect of PC or PCM plus laser on tumor cells, which was supported by the MTT results (Figure 4C). The main anticancer mechanism of CS-5 is to induce tumor cell apoptosis [11,40]. P53 can mediate cell apoptosis by regulating BCL-2 and Bax proteins [41]. The low expression of the proapoptotic protein Bcl-2 releases the restricted antiapoptotic protein of Bax to initiate apoptosis, and BAX induces the release of apoptotic factors such as caspase-3 to mediate the final cell death [42]. Western blot assay indicated that CS-5 significantly induced the expression of the proapoptotic proteins C-CASPASE-3, P53 and BAX, and inhibited the level of the antiapoptotic protein BCL-2 (Figure 4D). These results suggest that CS-5 played its role mainly by inducing the apoptosis of HCT116 cancer cells.

Ferroptosis mechanism *in vitro*

Recent studies have shown that CS-5 can induce ferroptosis [12], which is characterized by inducing ROS through the Fenton reaction and inhibiting the expression of MMP and GPX4 protein [15,43]. Therefore we used the JC-1 assay to detect the change in the MMP level. Red fluorescence and green fluorescence represented the normal MMP and the decreased MMP, respectively. The decrease in red fluorescence and increase in green fluorescence in the PCM + L group proved that CS-5 and PB plus laser could promote cell ferroptosis by inducing mitochondrial damage (Figure 5A). Meanwhile, fluorescence imaging indicated that CS-5 and PB plus laser could induce ROS generation. As we expected, PCM showed the most significant tumor cell-killing effect under laser induction (Figure 5B). It has been reported that inhibiting the expression of HSP70 protein can improve the sensitivity of cancer cells to PTT, thus improving the efficacy of tumor-cell ablation [44]. Therefore we detected the effect of PB on the expression of HSP70 protein. Consistent with previous reports [45,46], laser irradiation of PB significantly reduced the expression level of HSP70 protein in HCT116 cells ($p < 0.05$) (Figure 5C). In addition, HIF-1 α can reduce iron and ROS levels, which implies its universal role in anti-ferroptosis of other cancers [47,48]. PCM

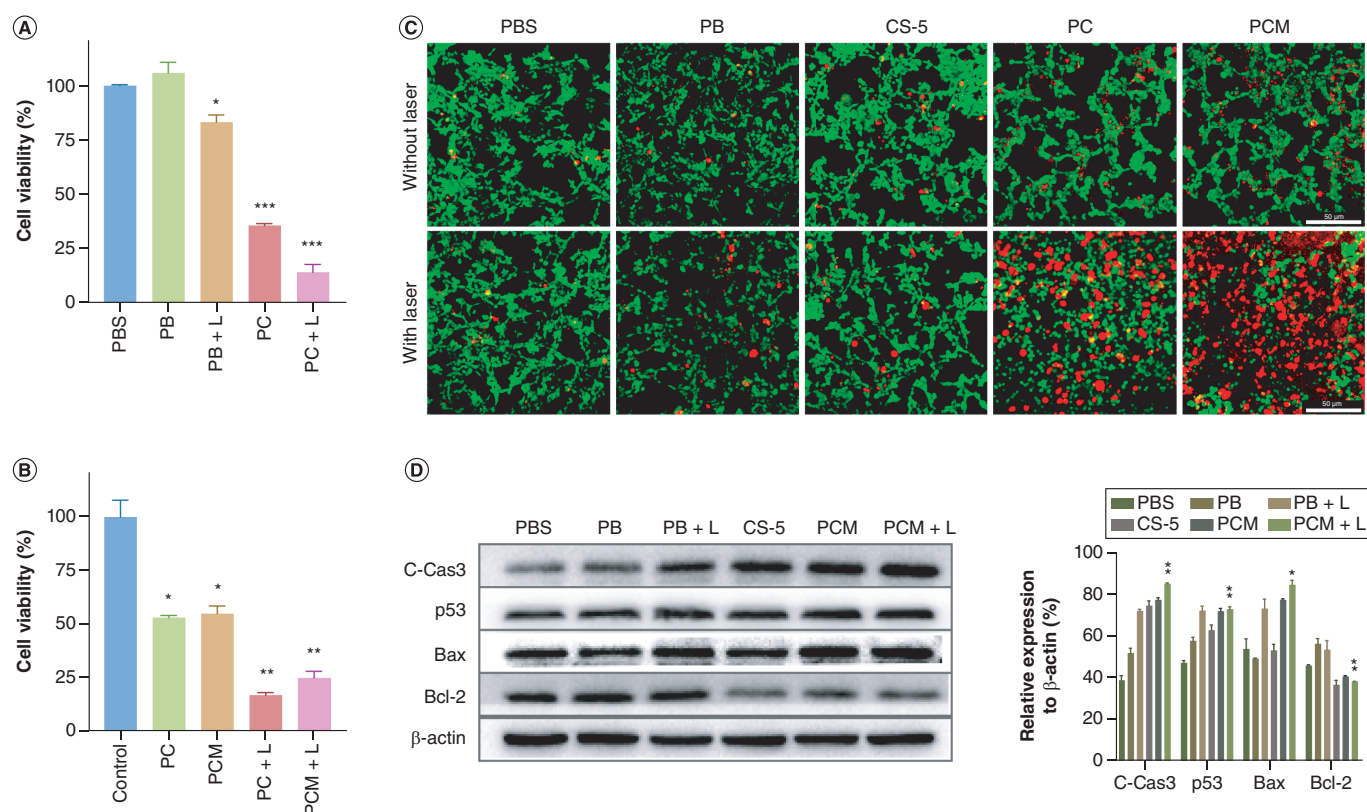


Figure 4. Antitumor effect and mechanism *in vitro*. (A) Comparison of the photothermal effect of PB and PC with or without laser (PBNPs = 30 μ g/ml, PB:CS-5 = 15:1) on HCT116 cells (* p < 0.05; *** p < 0.001). (B) Comparison of the photothermal effect of PC and PCM with or without laser (PBNPs = 30 μ g/ml, PB:CS-5 = 15:1) on HCT116 cells (* p < 0.05; ** p < 0.01). (C) Representative optical images of HCT116 cells with different treatments: PBS, PBS + L, PB, PB + L, CS-5, CS-5+L, PC, PC + L, PCM and PCM + L (scale bar = 50 μ m). Live cells (green); dead cells (red). (D) The expression and quantitative analysis of C-caspase-3, p53, Bax and Bcl-2 in HCT116 cells after different treatments at 24 h: PBS, CS-5, PB, PB+L, PCM and PCM+L (* p < 0.05; ** p < 0.01). CS-5: Buftotalin; L: Laser; PB: Prussian blue; PBNP: Prussian blue nanoparticle; PBS: Phosphate-buffered saline; PC: Buftotalin–Prussian blue nanoparticle; PCM: Buftotalin–Prussian blue biomimetic nanoparticle.

with laser can effectively reduce the expression of the ferroptosis-related proteins GPX4 and HIF-1 α (p < 0.01) (Figure 5D). These results indicated that PCM plus laser had a remarkable effect on ferroptosis by downregulating the levels of GPX4 and HIF-1 α proteins, inducing ROS production and reducing MMP.

Biodistribution & pharmacokinetics *in vivo*

To comprehensively evaluate the targeting ability of the hybrid membrane and metabolism of PB *in vivo*, 100 μ l of PB^{Ce6} and PB@M^{Ce6} (5 mg/kg PB) were injected into tumor-bearing mice via the tail vein, and the fluorescence signal distribution of Ce6 in tumor-bearing mice was monitored at different time points. As shown in Figure 6A, the fluorescence signal of Ce6 was found at the tumor site of mice administered PB^{Ce6} after 4 h but remained unchanged after 48 h in the PB@M^{Ce6} group (p < 0.05). After 48 h, the tumors and main organs were collected for fluorescence imaging. As shown in Figure 6B, the fluorescence signals were enriched in the tumor site of the mice, and the fluorescence intensity of PB@M^{Ce6} was significantly stronger than that of PB^{Ce6} (p < 0.05). This result demonstrated the excellent tumor-targeting ability of HCTm and the long half-life of RBCm. In addition, we found a strong fluorescence signal of PB^{Ce6} and PB@M^{Ce6} in the liver and kidney, as they are mainly metabolized through the liver and kidney (Figure 6C & D). Figure 6E & F show that the average serum half-lives of Ce6, PB^{Ce6} and PB@M^{Ce6} were 0.64, 1.43 and 1.63 h, respectively, indicating that RBCm could assist nanodrugs to escape the clearance of macrophages and prolong the half-life *in vivo*.

Antitumor effect *in vivo*

The chemotherapy/hyperthermia scheme of PCM on the mouse model of colorectal cancer is shown in Figure 7A.

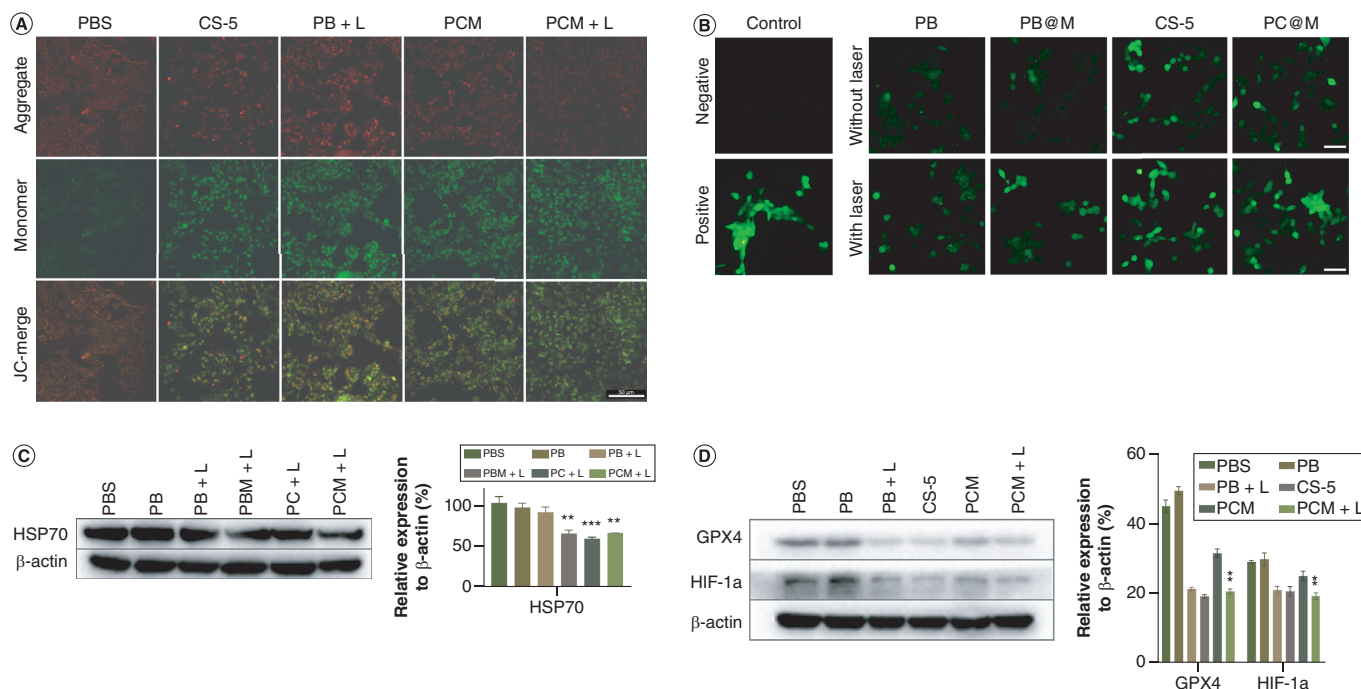


Figure 5. Ferroptosis mechanism *in vitro*. (A) The mitochondrial membrane potential (MMP) of HCT116 cells after incubation with PBS, CS-5, PBM+L, PCM and PCM+L using JC-1 assay; red represents normal MMP and green represents decreased MMP (scale bar = 50 μm). (B) Fluorescence images of ROS production after treatment with PB, PBM, CS-5 or PCM in HCT116 cells (scale bar = 20 μm). (C) The expression level and quantitative analysis of HSP70 after treatment with PBS, PB, PB+L, PBM+L, PC+L and PCM+L (**p < 0.01; ***p < 0.001). (D) The expression level and quantitative analysis of GPX4 and HIF-1a after the treatment with PBS, PB+L, PBM+L, CS-5, PCM and PCM+L (**p < 0.01).

CS-5: Bufotalin; L: Laser; PB: Prussian blue; PBM: PB@M; PBS: Phosphate-buffered saline; PC: Bufotalin–Prussian blue nanoparticle; PCM: Bufotalin–Prussian blue biomimetic nanoparticle; ROS: Reactive oxygen species.

When the tumor volume grew to 100 mm³, the mice were randomly divided into five groups: PBS, CS-5, PBM + L, PCM and PCM + L. First, we evaluated the photothermal conversion performance of different nanomaterials *in vivo*. After the tumor was irradiated by laser (808 nm, 1.2 w/cm²) for 5 min, the temperature of the tumor region with PBM and PCM administration reached 49.5°C (Figure 7B), indicating the excellent photothermal conversion performance and tumor targeting of PCM *in vivo*. On the contrary, mice treated with PBS did not show temperature change. After eight cycles of treatment, the tumor size of the PBS group gradually increased, and the maximal volume of the tumor was about 1800 cm³. Compared with the PBS group, the tumor growth in the CS-5, PBM + L and PCM groups was slightly inhibited, with inhibition rates of 41.16, 31.27 and 66.04%, respectively. The tumor growth in the PCM + L group was effectively controlled (p < 0.0001), with the highest inhibition rate of 87.97% (Figure 7C). The changing trend of relative tumor volume and tumor weight *in vivo* (Figure 7D–F & Supplementary Figure 5) is consistent with the therapeutic effect (p < 0.0001), and the body weight of mice had no significant changes (Figure 7G). These results proved the combined effects of PCM with laser on tumor growth inhibition.

To intuitively observe the antitumor mechanism *in vivo* of PCM + L, we performed H&E, TUNEL and immunohistochemical staining on tumor sections. H&E staining showed that a large number of necrotic tumor regions were observed in the PCM + L group. In TUNEL staining, compared with other groups, the PCM + L group showed the strongest green fluorescence, representing numerous apoptotic cells (Figure 7H). Compared with the PBS group, the protein levels of KI67, GPX4 and SLC7A11 in tumor tissues of the PCM + L group were significantly decreased. This result also confirmed that laser PCM can effectively inhibit tumor growth by inhibiting the expression of KI67 protein. In addition, the experimental results in Figure 7I indicated that CS-5 could downregulate the expression of GPX4 and SLC7A11 protein to induce ferroptosis in HCT116 cells, which also contributes to tumor growth inhibition. To sum up, PCM can achieve a satisfactory effect in chemo-photothermal therapy of colorectal cancer by inducing ferroptosis and apoptosis of HCT116 cells.

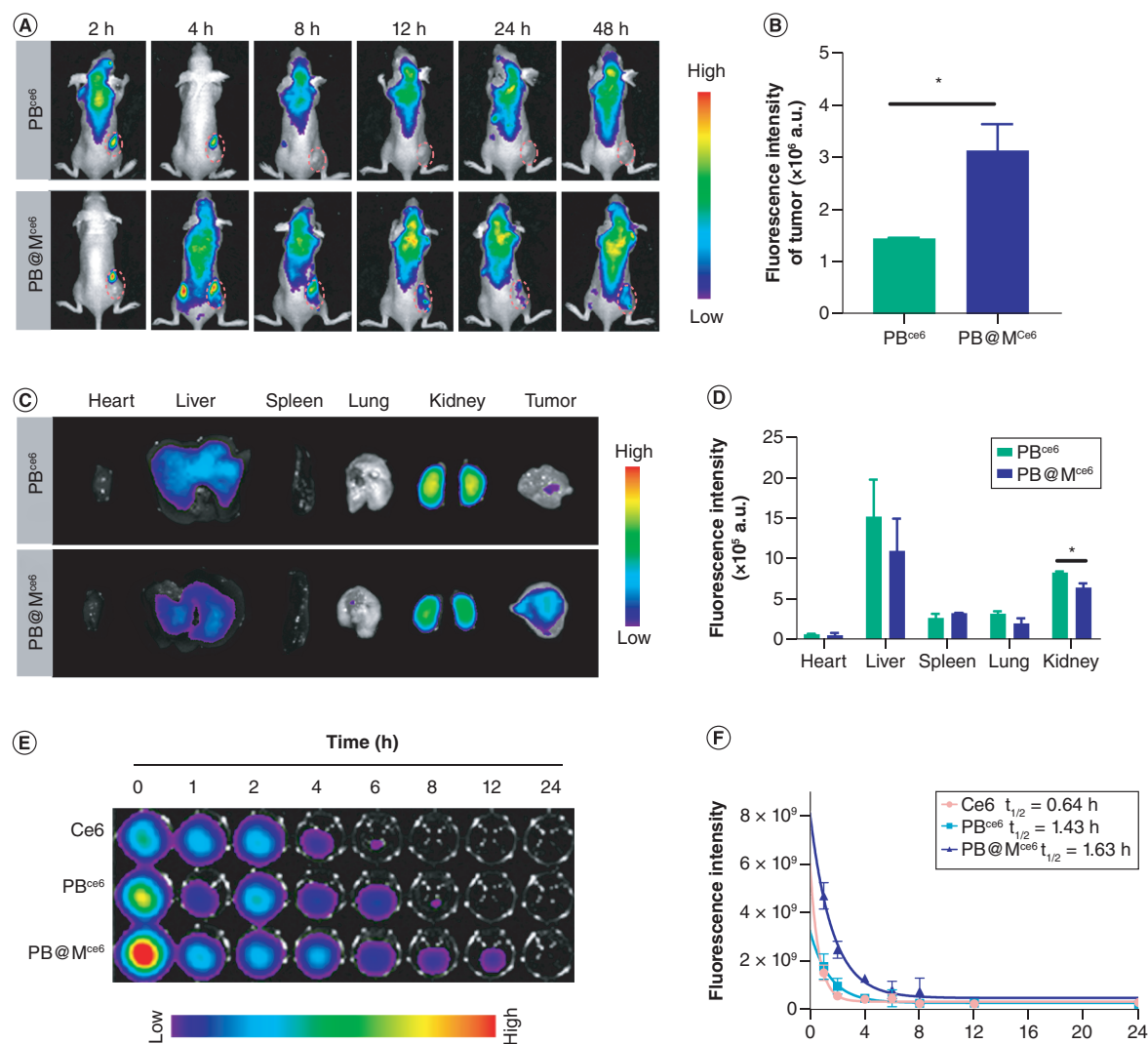


Figure 6. Biodistribution and pharmacokinetics *in vivo*. (A) Biodistribution and uptake of PB^{Ce6} and PB@M^{Ce6} in tumor-bearing BALB/c mice at different time points after intravenous injection. (B–D) Quantitative analysis of PB^{Ce6} and PB@M^{Ce6} in tumors and major organs (*p < 0.05). (E & F) Pharmacokinetic curves of Ce6, PB^{Ce6} and PB@M^{Ce6} after intravenous administration in tumor-bearing BALB/c mice. M: Membrane; PB: Prussian blue.

Biosafety assessment *in vivo*

To highlight the clinical application of PCM, H&E staining and routine blood and biochemical analysis were used to evaluate the biological safety of PCM in major organs (heart, liver, spleen, lung and kidney). H&E staining showed that different drug samples had no obvious toxic or side effects on main organs except that the cardiotoxicity of CS-5 might slightly increase the myocardial clearance compared with the PBS group (Supplementary Figure 6A). There were no differences in routine blood and biochemical tests among these groups, except for a slight increase of RBCs and platelets in the CS-5 group compared with the PBS group, which may relate to the poor prognosis of drug chemotherapy (Supplementary Figure 6B–F). In short, the PCM for chemo/thermotherapy demonstrated high biological safety, which is hopeful for developing clinical nanomedicine.

The comprehensive landscape of gut microbiota

Changes in the intestinal microbiota may relate to the curative effect of colon cancer therapy [49,50]. To investigate the role of microbiota on colon cancer therapy, 16S rRNA sequencing analysis was performed to investigate the intestinal microbiota change in mice after PCM + L treatment. Figure 8A indicates that the control group, PBS and PCM

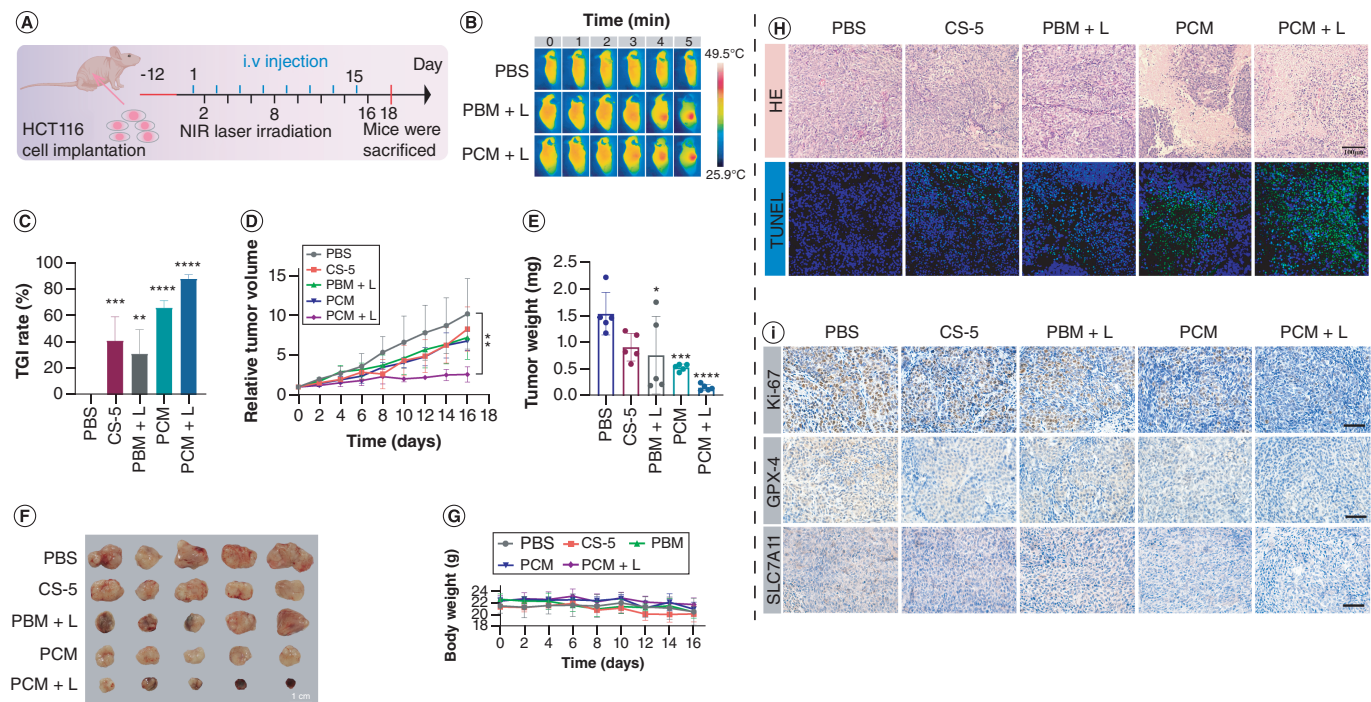


Figure 7. Buftotalin–Prussian blue biomimetic nanoparticles for dual-drug chemo-photothermal therapy *in vivo*. (A) The treatment regimen of the colorectal tumor model. (B) Infrared thermal image of mice within 5 min of near-infrared laser irradiation (1.2 W/cm²). (C) Tumor growth inhibition rate of tumor-bearing BALB/c mice among different groups: PBS, CS-5, PBM+L, PCM and PCM+L (***p* < 0.01; ****p* < 0.001; *****p* < 0.0001). (D) Relative tumor volume of mice with different treatments (***p* < 0.01). (E) The change of tumor weight of mice (**p* < 0.05; ****p* < 0.001; *****p* < 0.0001). (F) The images of tumors from the mice post treatment. (G) The body weight of mice. (H) Hematoxylin and eosin staining and terminal deoxynucleotidyl transferase dUTP nick end labeling assays of tumor tissues of tumor-bearing mice after different treatments: PBS, CS-5, PBM+L, PCM and PCM+L (scale bar = 100 μm). (I) Immunohistochemical staining of Ki67, GPX4 and SLC7A11 in tumor tissues with different treatments: PBS, CS-5, PBM+L, PCM and PCM+L (scale bar = 100 μm). CS-5: Buftotalin; L: Laser; PBM: PB@M; PBS: Phosphate-buffered saline; PCM: Buftotalin–Prussian blue biomimetic nanoparticle; TGI: Tumor growth inhibition.

+ L group shared 353 of the total 2727 operational taxonomy units (OTUs), the PBS and PCM + L group shared 885 OTUs, and 485 OTUs were unique to the PCML group. The α -diversity of intestinal microbiota was evaluated using Chao1 and OTU indexes, and the results showed that species diversity in the PBS and PCM + L groups was significantly higher than that of the control group (Figure 8B & C). The abundance distribution of intestinal microbiota was demonstrated with a Circos plot and heat map (Figure 8D & E). Compared with the control group and PBS group, the abundance of *Helicobacter pylori*, *Ricardia* and *Streptococcus* in the PCM + L group increased, while the abundance of *Candidatus saccharimonas*, *Anaerotruncus*, *HT002* and *Enterorhabdus* decreased. Moreover, the indicator analysis was conducted to screen indicative microbiota biomarkers. Compared with the control group, Chloroflexi, Myxococcota, Gemmatimonadota, WPS-2, Campylobacterota and Proteobacteria were significantly enriched in PBS and PCM + L groups, which may serve as biomarkers for colon cancer detection. Nitrospirata and NB1-j were significantly enriched in the PCM + L group, which may serve as a biomarker for evaluating the efficacy of tumor therapy (Supplementary Figure 7A), and a branch map was drawn to identify specific intestinal microflora (Supplementary Figure 7B). In addition, the PICRUST2 method was used to predict the microbial population function in the PCM + L treatment group across the pathway database (Supplementary Figure 7C). The results indicated that the pentose phosphate pathway and superpathway of pyrimidine deoxyribonucleotides *de novo* biosynthesis are significantly related to the PCM + L with the potential of anticancer drug targeting.

Discussion

In this study, PBNPs with stable and uniform particle sizes were synthesized based on an economical and fast hydrothermal method. The nanomaterial has an excellent near-infrared photothermal conversion effect and has great potential as a new generation substitute for traditional photothermal agents. More importantly, its high

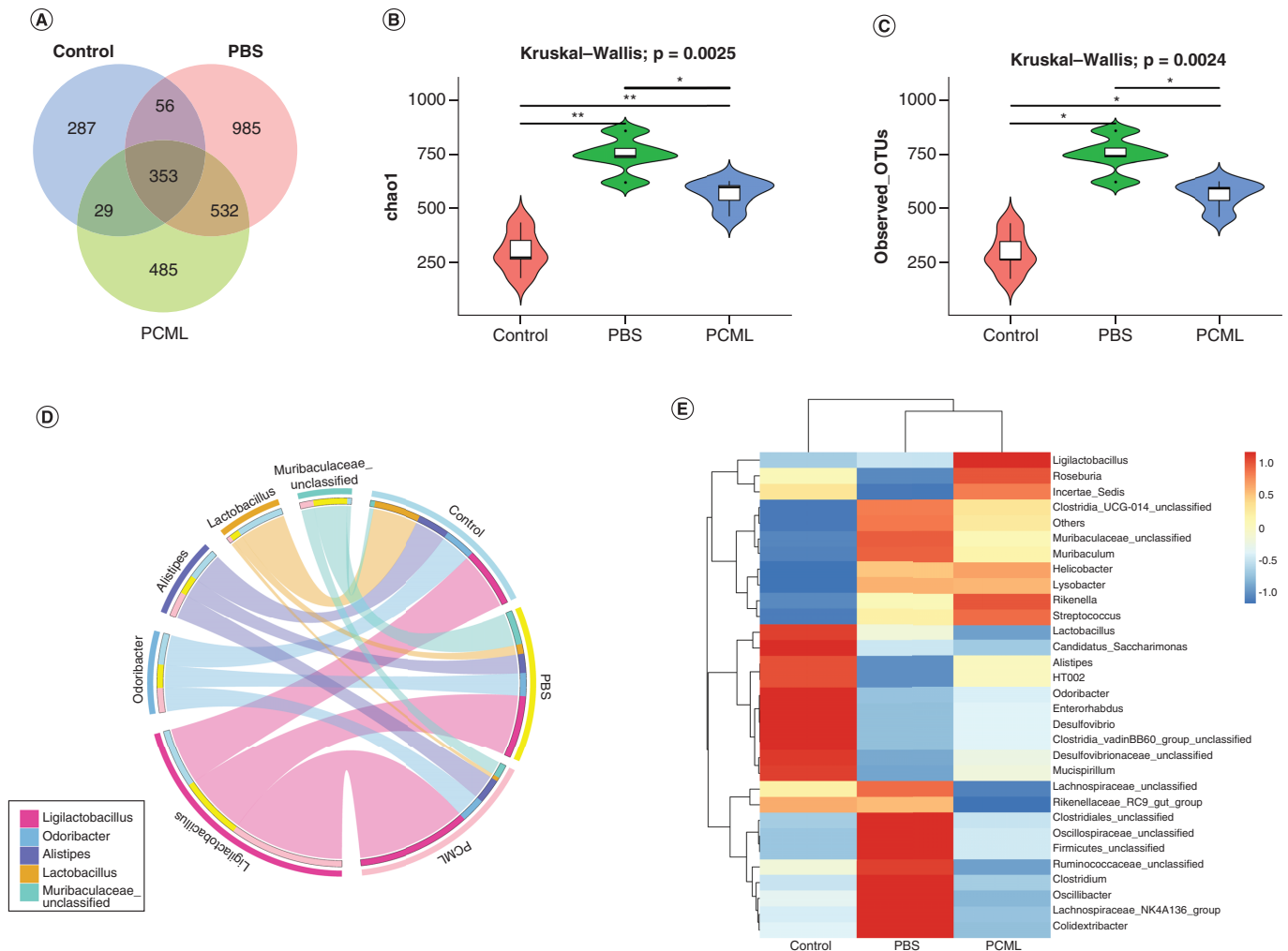


Figure 8. Gut microbiota distribution and composition based on the 16S rRNA gene amplicon sequencing. **(A)** Venn diagram of the distribution differences of OTUs in control, PBS and PCM + L groups. **(B & C)** The α -diversity of gut microbiota was estimated by **(B)** the Chao1 and **(C)** the observed species indexes (* $p < 0.05$; ** $p < 0.01$). **(D)** Circos plot at the genus level. The left side of the circle represents species and the right side represents different groups. **(E)** The heat map of abundance distribution of gut microbiota in three groups with the top 30 species at the genus level.

L: Laser; OTU: Operational taxonomy unit; PBS: Phosphate-buffered saline; PCM: Buftotalin-Prussian blue biomimetic nanoparticle.

drug-loading rate and biosafety have attracted more attention in cancer treatment. Therefore, we constructed a biomimetic drug-delivery system, PCM, and comprehensively evaluated its thermo-chemotherapy efficacy in colorectal cancer.

Firstly, the performance of the material was given prior consideration. The drug loading and biomimetic membrane modification did not affect the photothermal properties of PB, and its photothermal conversion efficiency is 31.33%, better than many photothermal agents. The modification with biomimetic membranes endows PC with higher blood compatibility and biosafety. In addition, PCM can be triggered by the dual mode of near-infrared and pH transition (tumor cell environment) to achieve on-demand release.

Secondly, the anticancer effect and mechanism of PCM were verified at the cellular level. The therapeutic efficacy of PCM combined with laser is better than that of PC or PB with laser. The anticancer mechanism of PCM can be summarized in two aspects. On one hand, CS-5 can regulate the expression of apoptosis-related proteins and induce apoptosis of colorectal cancer cells; on the other hand, CS-5 can downregulate ferroptosis-related proteins (GPX4 and HIF-1a) and induce the production of ROS to finally realize ferroptosis in the colorectal cancer cell.

Finally, the biosafety, anticancer efficacy and mechanism of PCM were also investigated *in vitro*. The combination of PCM and laser can significantly inhibit tumor growth (tumor inhibition rate up to 87.97%) and ablate tumors.

The results of immunohistochemistry and TUNEL staining also further verified the ability of PCM to induce apoptosis and ferroptosis in HCT116 cells. Blood routine and biochemical indicators also indicated the biosafety of PCM. 16S rRNA sequencing analysis screened the possible therapeutic indicators and related pathways for colorectal cancer, which may provide new ideas for clinical prognosis and drug mechanism research. In general, PCM is a ferroptosis-related thermochemotherapy biomimetic nanomedicine possessing high safety and low toxicity and side effects, which implies its broad clinical application prospects.

Conclusion

In this study, we constructed a biomimetic nanomedicine, PCM, which has good biocompatibility, tumor-targeting and laser-responsive properties, and can be used effectively for chemo/thermotherapy against colon cancer. The nanomedicine has the following prominent advantages. First, the hybrid membrane of RBCm-HCTm could prolong the blood circulation time of the nanomedicine, target the tumor site accurately and reduce the cardiotoxicity of CS-5 in chemotherapy. Second, the nanomedicine can be used as a ferroptosis inducer to downregulate the expression of GPX4 and HIF-1 α proteins, upregulate ROS production and reducing MMP. Third, the high temperature caused by laser irradiation can improve the therapeutic effect by accelerating the release of CS-5 and iron and ferrous ions from PBNPs. To sum up, the chemotherapeutic effect of CS-5 combined with the photothermal effect of PB can effectively treat colon cancer by inducing ferroptosis. However, the precise dosage of CS-5 needs further optimization.

Based on the work results of PCM in the treatment of colorectal cancer, the current research is limited, and there is still a wide range of research space worth exploring:

- (1) Chemotherapy with CS-5 in colorectal cancer may induce cell resistance. In the future, PB-loaded dual medicine combined with PTT for colorectal cancer may solve this issue.
- (2) Studies have shown that CS-5 can inhibit tumor metastasis and invasion. In our future work, animal models of tumor metastasis and invasion may be considered. Moreover, the specific pathways involved in CS-5-induced ferroptosis in colorectal cancer cells may be further verified.

Summary points

- The precision control of the size of bufotalin–Prussian blue biomimetic nanoparticles (PB@CS-5@M; PCM; 128.3 nm) contributes to its tumor targeting and rapid metabolism to the exterior.
- PCM has the potential for on-demand release under the trigger of near-infrared and pH transition (tumor cell environment).
- The modification with hybrid red blood cell/HCT116 cell membranes could prolong the blood circulation time of PCM, reduce the cardiotoxicity of CS-5 in chemotherapy and achieve precise targeting of tumors.
- Prussian blue (PB) can significantly inhibit the expression of HSP70 under laser irradiation to improve the sensitivity of colorectal cancer cells to photothermal therapy, thus improving the efficacy of tumor ablation.
- CS-5 may serve as a new ferroptosis inducer for antitumor therapy with the assistance of thermotherapy in the production of reactive oxygen species and the release of Fe²⁺ from PB.
- PCM had a remarkable effect on ferroptosis by downregulating the levels of GPX4 and HIF-1 α proteins, inducing reactive oxygen species production and reducing mitochondrial membrane potential.

Supplementary data

To view the supplementary data that accompany this paper please visit the journal website at: www.futuremedicine.com/doi/suppl/10.2217/nnm-2023-0293

Author contributions

Y Wu and J Tian were responsible for experimental design, overall experimental verification, data processing and article writing. M Luo and Z Wu revised and verified the experimental data. R Cao drew the schematic diagram and was responsible for the beautification of all figures. JY and Q Peng were responsible for drug-efficacy verification *in vitro*. R Liu and Y Qiu were responsible for experimental design, format modification and manuscript revision.

Acknowledgments

The authors sincerely thank all funding providers, research fund projects and the experimental platform provided by the College of Biology, Hunan University.

Financial disclosure

This research was funded by the Hunan Provincial Key Research and Development Program (No. 2019SK2042), the National Natural Science Foundation of China (no. 31072141, no.12034006), and the Applied Basic Research Project of Changzhou Science and Technology Bureau (no. 202202086). The authors have no other relevant affiliations or financial involvement with any organization or entity with a financial interest in or financial conflict with the subject matter or materials discussed in the manuscript apart from those disclosed. This includes employment, consultancies, honoraria, stock ownership or options, expert testimony, grants or patents received or pending, or royalties.

Competing interests disclosure

The authors have no competing interests or relevant affiliations with any organization or entity with the subject matter or materials discussed in the manuscript. This includes employment, consultancies, honoraria, stock ownership or options, expert testimony, grants or patents received or pending, or royalties.

Writing disclosure

No writing assistance was utilized in the production of this manuscript.

Ethical conduct of research

All animal experiments were carried out at the Laboratory Animal Center of Hunan Normal University School of Medicine, and all experiment protocols conform to the principles of the Declaration of Helsinki of the Ministry of Health (approval no. D2022012).

Open access

This work is licensed under the Attribution-NonCommercial-NoDerivatives 4.0 Unported License. To view a copy of this license, visit <http://creativecommons.org/licenses/by-nc-nd/4.0/>

References

- Bhimani N, Wong GY, Molloy C, Dieng M, Hugh TJ. Cost of colorectal cancer by treatment type from different health economic perspectives: a systematic review. *Eur. J. Surg. Oncol.* 48(10), 2082–2093 (2022).
- Siegel RL, Miller KD, Fuchs HE, Jemal A. Cancer statistics, 2022. *CA Cancer J. Clin.* 72(1), 7–33 (2022).
- Martelli V, Pastorino A, Sobrero AF. Prognostic and predictive molecular biomarkers in advanced colorectal cancer. *Pharmacol. Ther.* 236, 108239 (2022).
- Lee S-Y, An M, Lee J. Immune landscape of colorectal cancer lung metastasis. *J. Clin. Oncol.* 40(16), e15542 (2022).
- Singh P, Waghambare P, Khan TA, Omri A. Colorectal cancer management: strategies in drug delivery. *Expert Opin. Drug Deliv.* 19(6), 653–670 (2022).
- Luo M, Yang X, Chen HN, Nice EC, Huang C. Drug resistance in colorectal cancer: an epigenetic overview. *Biochim. Biophys. Acta Rev. Cancer* 1876(2), 188623 (2021).
- Folprecht G, Martinelli E, Mazard T *et al.* Triplet chemotherapy in combination with anti-EGFR agents for the treatment of metastatic colorectal cancer: current evidence, advances, and future perspectives. *Cancer Treat. Rev.* 102, 102301 (2022).
- Karthika C, Hari B, Rahman MH *et al.* Multiple strategies with the synergistic approach for addressing colorectal cancer. *Biomed. Pharmacother.* 140, 111704 (2021).
- Bekaii-Saab T, Kim R, Kim TW *et al.* Third- or later-line therapy for metastatic colorectal cancer: reviewing best practice. *Clin. Colorectal Cancer* 18(1), e117–e129 (2019).
- Dai ZR, Ning J, Sun GB *et al.* Cytochrome P450 3A enzymes are key contributors for hepatic metabolism of bufotalin, a natural constituent in Chinese medicine Chansu. *Front. Pharmacol.* 10, 2409–2417 (2019).
- Pan ZH, Qu CJ, Chen Y *et al.* Bufotalin induces cell cycle arrest and cell apoptosis in human malignant melanoma A375 cells. *Oncol. Rep.* 41(4), 2409–2417 (2019).
- Zhang W, Jiang BP, Liu YX, Xu L, Wan M. Bufotalin induces ferroptosis in non-small cell lung cancer cells by facilitating the ubiquitination and degradation of GPX4. *Free Radic. Biol. Med.* 180, 75–84 (2022).
- Zhang DM, Liu JS, Tang MK *et al.* Bufotalin from *Venenum bufonis* inhibits the growth of multidrug resistant HepG2 cells through G(2)/M cell cycle arrest and apoptosis. *Eur. J. Pharmacol.* 692(1–3), 19–28 (2012).

14. Cao JY, Dixon SJ. Mechanisms of ferroptosis. *Cell. Mol. Life Sci.* 73(11-12), 2195–2209 (2016).
15. Chen GH, Song CC, Pantopoulos K, Wei XL, Zheng H, Luo Z. Mitochondrial oxidative stress mediated Fe-induced ferroptosis via the NRF2-ARE pathway. *Free Radic. Biol. Med.* 180, 95–107 (2022).
16. Chen X, Kang R, Kroemer G, Tang DL. Broadening horizons: the role of ferroptosis in cancer. *Nat. Rev. Clin. Oncol.* 18(5), 280–296 (2021).
17. Qiu Y, Cao Y, Cao W, Jia Y, Lu N. The application of ferroptosis in diseases. *Pharmacol. Res.* 159, 104919 (2020).
18. Du YQ, Zhang R, Yang JN *et al.* A 'closed-loop' therapeutic strategy based on mutually reinforced ferroptosis and immunotherapy. *Adv. Funct. Mater.* 32(13), 2111784 (2022).
19. Guo P, Huang J, Moses MA. Cancer nanomedicines in an evolving oncology landscape. *Trends Pharmacol. Sci.* 41(10), 730–742 (2020).
20. Wang YQ, Li SM, Wang XH *et al.* Smart transformable nanomedicines for cancer therapy. *Biomaterials* 271, 120737 (2021).
21. Iranpour S, Bahrami AR, Saljooghi AS, Martin MM. Application of smart nanoparticles as a potential platform for effective colorectal cancer therapy. *Coord. Chem. Rev.* 442, 213949 (2021).
22. Guan Q, Guo R, Huang S *et al.* Mesoporous polydopamine carrying sorafenib and SPIO nanoparticles for MRI-guided ferroptosis cancer therapy. *J. Control. Rel.* 320, 392–403 (2020).
23. Wang XW, Cheng L. Multifunctional Prussian blue-based nanomaterials: preparation, modification, and theranostic applications. *Coord. Chem. Rev.* 419, 213393 (2020).
24. Busquets MA, Estelrich J. Prussian blue nanoparticles: synthesis, surface modification, and biomedical applications. *Drug Discov. Today* 25(8), 1431–1443 (2020).
25. Chen J, Xue F, Du W *et al.* An endogenous H₂S-activated nanoplatform for triple synergistic therapy of colorectal cancer. *Nano Lett.* 22(15), 6156–6165 (2022).
26. Xing L, Liu XY, Zhou TJ, Wan X, Wang Y, Jiang HL. Photothermal nanozyme-ignited Fenton reaction-independent ferroptosis for breast cancer therapy. *J. Control. Rel.* 339, 14–26 (2021).
27. Sun LL, Xiong ZJ, Shen FY, Wang ZH, Liu Z. Biological membrane derived nanomedicines for cancer therapy. *Sci. China Chem.* 64(5), 719–733 (2021).
28. Fang RH, Kroll AV, Gao WW, Zhang LF. Cell membrane coating nanotechnology. *Adv. Mater.* 30(23), e1706759 (2018).
29. Xiao C, Tong CY, Fan JL *et al.* Biomimetic nanoparticles loading with gambutolin-indomethacin for chemo/photothermal therapy of cervical cancer and anti-inflammation. *J. Control. Rel.* 339, 259–273 (2021).
30. Liang J, Wang C, Fan J *et al.* Hybrid membrane-camouflaged hollow Prussian blue nanoparticles for shikonin loading and combined chemo/photothermal therapy of metastatic TNBC. *Mater. Today Adv.* 14, 100245 (2022).
31. Zheng DY, Yu PW, Wei ZW, Zhong C, Wu M, Liu XL. RBC membrane camouflaged semiconducting polymer nanoparticles for near-infrared photoacoustic imaging and photothermal therapy. *Nano Micro Lett.* 12(1), 94 (2020).
32. Chen HL, Zheng DH, Pan WZ *et al.* Biomimetic nanotheranostics camouflaged with cancer cell membranes integrating persistent oxygen supply and homotypic targeting for hypoxic tumor elimination. *ACS Appl. Mater. Interfaces* 13(17), 19710–19725 (2021).
33. Peng X, Wang R, Wang TJ *et al.* Carbon dots/Prussian blue satellite/core nanocomposites for optical imaging and photothermal therapy. *ACS Appl. Mater. Interfaces* 10(1), 1084–1092 (2018).
34. Yao DF, Wang YS, Zou RF *et al.* Molecular engineered squaraine nanoprobe for NIR-II/photoacoustic imaging and photothermal therapy of metastatic breast cancer. *ACS Appl. Mater. Interfaces* 12(4), 4276–4284 (2020).
35. Wu X, Chen GY, Owens G, Chu DW, Xu HL. Photothermal materials: a key platform enabling highly efficient water evaporation driven by solar energy. *Mater. Today Energy* 12, 277–296 (2019).
36. Fu JJ, Wu B, Wei MY *et al.* Prussian blue nanosphere-embedded *in situ* hydrogel for photothermal therapy by peritumoral administration. *Acta Pharm. Sin. B* 9(3), 604–614 (2019).
37. Wang P, Kankala RK, Chen BQ *et al.* Cancer cytomembrane-cloaked Prussian blue nanoparticles enhance the efficacy of mild-temperature photothermal therapy by disrupting mitochondrial functions of cancer cells. *ACS Appl. Mater. Interfaces* 13(31), 37563–37577 (2021).
38. Chen HY, Deng J, Wang Y, Wu CQ, Li X, Dai HW. Hybrid cell membrane-coated nanoparticles: a multifunctional biomimetic platform for cancer diagnosis and therapy. *Acta Biomater.* 112, 1–13 (2020).
39. Le QV, Lee J, Lee H, Shim G, Oh YK. Cell membrane-derived vesicles for delivery of therapeutic agents. *Acta Pharm. Sin. B* 11(8), 2096–2113 (2021).
40. Lin S, Lv J, Peng P *et al.* Bufadienolides induce p53-mediated apoptosis in esophageal squamous cell carcinoma cells *in vitro* and *in vivo*. *Oncol. Lett.* 15(2), 1566–1572 (2018).
41. Basu A. The interplay between apoptosis and cellular senescence: bcl-2 family proteins as targets for cancer therapy. *Pharmacol. Ther.* 230, 107943 (2022).

42. Dadsena S, King LE, García-Sáez AJ. Apoptosis regulation at the mitochondria membrane level. *Biochim. Biophys. Acta Biomembr.* 1863(12), 183716 (2021).
43. Jelinek A, Heyder L, Daude M *et al.* Mitochondrial rescue prevents glutathione peroxidase-dependent ferroptosis. *Free Radic. Biol. Med.* 117, 45–57 (2018).
44. Wang ZH, Li SW, Zhang M *et al.* Laser-triggered small interfering RNA releasing gold nanoshells against heat shock protein for sensitized photothermal therapy. *Adv. Sci.* 4(2), 1600327 (2017).
45. Liu YJ, Shu GM, Li X *et al.* Human HSP70 promoter-based Prussian blue nanotheranostics for thermo-controlled gene therapy and synergistic photothermal ablation. *Adv. Funct. Mater.* 28, 662 (2018).
46. Tian BS, Wang C, Du YQ *et al.* Near infrared-triggered theranostic nanoplatfrom with controlled release of HSP90 inhibitor for synergistic mild photothermal and enhanced nanocatalytic therapy with hypoxia relief. *Small* 18(7), e2200786 (2022).
47. Henning Y, Blind US, Larafa S, Matschke J, Fandrey J. Hypoxia aggravates ferroptosis in RPE cells by promoting the Fenton reaction. *Cell Death Dis.* 13, 662 (2022).
48. Lin Z, Song J, Gao Y *et al.* Hypoxia-induced HIF-1 α /lncRNA-PMAN inhibits ferroptosis by promoting the cytoplasmic translocation of ELAVL1 in peritoneal dissemination from gastric cancer. *Redox Biol.* 52, 102312 (2022).
49. Zhang HB, Yu YH, Li JH *et al.* Changes of gut microbiota in colorectal cancer patients with *Pentatrichomonas hominis* infection. *Front. Cell. Infect. Microbiol.* 12, 961974 (2022).
50. Martinez-Montoro JI, Martinez-Sanchez MA, Balaguer-Roman A *et al.* Dietary modulation of gut microbiota in patients with colorectal cancer undergoing surgery: a review. *Int. J. Surg.* 104, 106751 (2022).